Earth Planets Space, **54**, 1153–1171, 2002

Hydraulic diffusivity of fault gouge zones and implications for thermal pressurization during seismic slip

Christopher A. J. Wibberley

Department of Geology and Mineralogy, Graduate School of Science, Kyoto University, Kyoto 606-8502, Japan

(Received February 13, 2002; Revised August 6, 2002; Accepted September 30, 2002)

Laboratory-determined permeability and compressibility data for natural fault gouge samples from the Median Tectonic Line (MTL) are presented and used to estimate hydraulic diffusivities in fault gouge zones. Bulk compressibility varies with effective pressure in a log-linear manner. Hydraulic diffusivity decreases significantly during the first isotropic loading partly due to a plastic compaction component, but does not significantly change during elastic unloading. Hydraulic diffusivity decreases with decreasing gouge grain size and is lowest in the very fine-grained centre of the fault zone, identified as the most recent principal displacement zone of the MTL. Previous models of fluid-controlled dynamic strength evolution during seismic slip are assessed using the data. The data suggest that the most recent principal displacement zone has a characteristic hydraulic diffusion length lower than the half width of the low-permeability zone. Hence pressurized fluid is unlikely to escape into the surrounding high-permeability fault rocks over the lifetime of an earthquake slip event, suggesting that thermal pressurization is likely to occur if the rupture plane is confined to the low-permeability gouge principal displacement zone.

1. Introduction

Shear zone fluid pressure has been highlighted in conceptual and theoretical models for the past 30 years or so as controlling fault strength changes during earthquake slip, and hence overall stress release during the earthquake (e.g. Sibson, 1973; Lachenbruch, 1980; Hickman *et al.*, 1995). However, there is still a great need to have data to constrain these models, especially because of the importance of such models in predicting earthquake magnitudes and reoccurrence times (e.g. Miller, 2002). One of the most important parameters in such models is hydraulic diffusivity, which is controlled by the permeability and fluid-pore compressibility of the fault zone material, and by fluid viscosity. Indeed, in theoretical studies of the thermal pressurization model of slip weakening, Lachenbruch (1980) and Mase and Smith (1987) both identified permeability as being one of the most influential and uncertain physical parameters of fault zone materials at relevant depths.

Previous laboratory works on fluid flow properties of natural fault gouges have shown that fault gouge generally has a low permeability with a significant anisotropy in permeability (e.g. Chu *et al.*, 1981; Morrow *et al.*, 1981, 1984; Faulkner and Rutter, 2000). Recently however, a few studies using well-defined structural context have encompassed other types of fault rocks and the general permeability structure of fault zones (Evans *et al.*, 1997; Seront *et al.*, 1998; Wibberley and Shimamoto, 2003). These integrated studies have shown that gouge zones forming a fault 'core' tend to have permeabilities significantly lower than surrounding 'damage zone' fault rocks, notably cataclasites and zones of fractured protolith, in fault zones modelled by Caine *et al.* (1996) as being a dual conduit/barrier system. This simple model is consistent with observations on internal structure of the Nojima fault zone (e.g. Ohtani *et al.*, 2001; Kobayashi *et al.*, 2001), laboratory-determined low permeability of Nojima gouge cores (Lockner *et al.*, 2000; Mizoguchi *et al.*, 2000) and high fault-parallel permeability determined from in situ water injection experiments (Tadokoro *et al.*, 2001) in which water was probably migrating in the fracture damage zone. However, assessing the hydrodynamic behaviour of the core zone during rapid slip requires more detailed examination of the permeability and poro-elastic properties and their variations with effective pressure. This paper aims to present such an examination for the first time, with the additional constraint that the samples were collected from in and around a narrow principal displacement zone within a much wider core of a large fault zone (Wibberley and Shimamoto, 2003).

2. The Median Tectonic Line Gouge Zone

The Median Tectonic Line is Japan's largest onshore fault (Fig. 1(a)) with a history of sinistral displacement dating back to the early Cretaceous (e.g. Ichikawa, 1980). Ryoke terrain mylonites juxtaposed against Sambagawa terrain schists have yielded a variety of fault rocks at different temperatures and pressures during the deformation and exhumation history of the Median Tectonic Line (e.g. Takagi, 1986). Miocene-onwards dextral reactivation has occurred on the Median Tectonic Line, but the fault is currently active only in Shikoku and the western part of the Kii Peninsula. Excellent exposure of the fault zone near Tsukide in western Mie Prefecture (Fig. 1(b)) shows that a significant

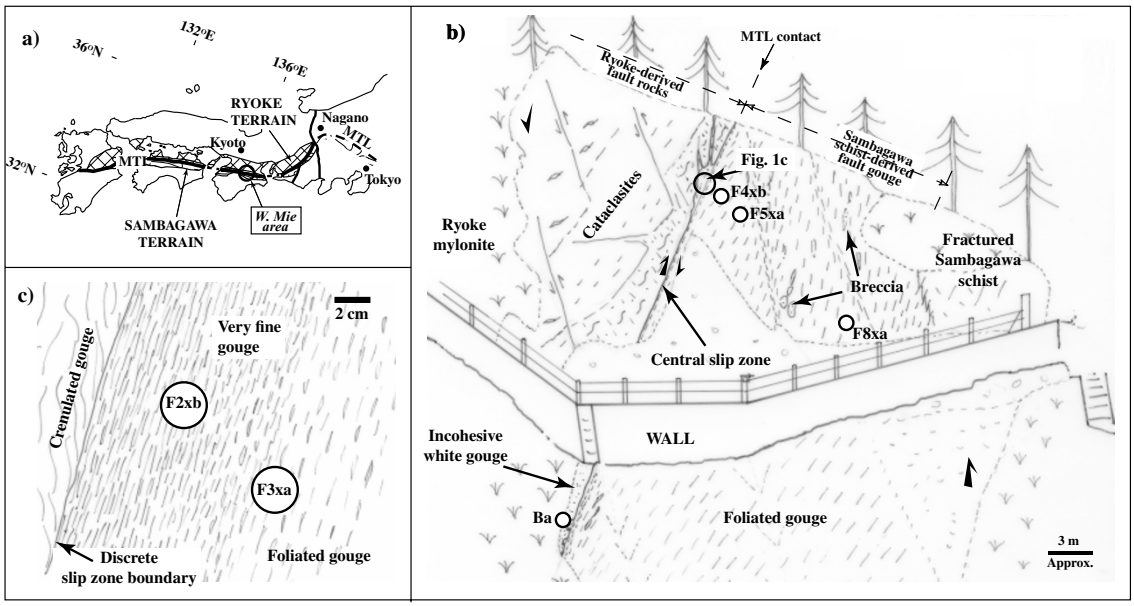

Fig. 1. Structural context of the gouge slip zone studied. (a) Regional map of the Median Tectonic Line. (b) Sketch of the upper portion of the Tsukide exposure of the Median Tectonic Line fault zone in western Mie Prefecture, showing the locations of samples. (c) Close-up sketch of the central slip zone, showing the location of samples taken.

Table 1. Details of samples used in this study for permeability measurements.

Fault rock type	Sample name	Fault-perpendicular distance from slip zone boundary (m)	Weight % of grains >250 μm
Coarse white gouge	Ba	−0.45	58.4
Very fine gouge	F2xb	0.05	3.74
Foliated gouge	F3xa	0.1	23.2
Foliated gouge	F4xb	0.35	34.5
Foliated gouge	F5xa	1.05	38.4
Coarse foliated gouge	F8xa	11.8	75.3

portion of the fault rocks in the central 'core' zone are foliated gouges, derived from Sambagawa schist (Wibberley and Shimamoto, 2003). At the contact with Ryoke-derived fault rocks, a 10 cm wide dextral slickenside-bounded planar zone of intensely sheared gouge termed 'central slip zone' (Figs. 1(b), (c)) cross-cuts all other structures, and is interpreted to represent the principal displacement zone of the most recent, possibly seismogenic, deformation.

Previous work on the overall permeability structure of the fault zone from laboratory room temperature experiments (Wibberley and Shimamoto, 2003) has shown that gouges from the central slip zone have the lowest permeabilities of all the fault rocks. For the gouges, grain size correlates well with permeability, both of which decrease inwards systematically from the edge of the fault zone to the central slip zone (Table 1). All these gouges consist of a phyllosilicate matrix-supported quartz clast fabric, with both clast size and proportion varying considerably (Wibberley and Shimamoto, 2003). The central slip zone gouges contain quartz clasts which are both very small and of low proportion relative to the clay matrix. The coarse foliated gouge has a high proportion of quartz clasts which are also much larger, almost providing a clast-supported framework. XRD work determined the matrix composition as being dominated by illite/muscovite, and no wetting clays were detected. The work described in this paper has determined not only permeability data of the gouges at and around the central slip zone in more detail than Wibberley and Shimamoto (2003), but fluid storage and compressibility data as well, in order to estimate likely hydraulic diffusivities of the gouges. The gouge samples used in this study (Table 1) are located in the outcrop sketches (Figs. 1(b), (c)), with the 'F-series' being black foliated gouges and very fine-grained slip zone gouge (F2 being the finest in the centre of the slip zone and F8 being the coarsest towards the edge of the fault zone), and coarse white gouge (Ba).

3. Experimental Methodology

The experiments described in this paper were performed using the high pressure deformation and fluid flow gas apparatus at Kyoto University. Samples were collected parallel to gouge foliation by hammering 25 mm internal diameter steel tubes (thinned to a wall thickness of about 0.5 mm) into the gouge outcrop and directly transferring them to polyolefin

jackets stoppered with porous end pieces. The samples were oven dried at 80°C to eliminate pore water, without removing structured water adsorbed onto clay mineral surfaces. After removing the stoppers, each of the samples was then placed between perforated brass spacers and further jacketed with the end pistons before being inserted into the pressure vessel of the gas rig.

Nitrogen gas was used both as a confining medium and a pore fluid. The samples were subjected to initial confining and pore fluid pressures of 20 MPa. The confining pressure (Pc) was then increased in steps up to a peak pressure of 200 MPa, and decreased in steps back to 20 MPa. During each confining pressure step, the change in pore volume of the sample was measured with a volumometer under 'drained' conditions. By assuming that the pore volume change (ΔVp) in the sample represented the entire volume change (i.e. that the mineral phases are relatively incompressible in comparison to the pores), pore volume change data were used to calculate total sample volumetric strain. At the beginning and end of each confining pressure step, the piston position at which incipient loading of the sample occurs ('hitpoint') was measured, and the difference taken as an estimate of the change in sample length during each confining pressure step. Axial strains were calculated from the piston displacement data. After each confining pressure step, permeability (k) and sample storage capacity (β_c) measurements were made using the oscillating pore pressure technique (Kranz *et al.*, 1990; Fischer and Paterson, 1992). In this way, a set of data was obtained for a complete confining pressure cycle for each sample. For the higher permeability samples (samples Ba, F8 and F5) some additional measurements were carried out at a pore pressure (Pp) of 30 MPa. Sample bulk framework compressibility (β_b) during each confining pressure step was calculated by finding the volume change per unit confining pressure increase, and dividing this by the sample volume at the start of the confining pressure step. This method only gives an 'average' compressibility over the Pc range of the step, which can be assumed to represent the compressibility at the median Pc of the step (Fig. 2). Such compressibility data, not presented later, tend to show a log-linear relationship with Pc. In order to obtain compressibility values relating to the same confining pressure conditions as the oscillating pore pressure measurements, it was necessary to perform an extrapolation between two median compressibility values (e.g. extrapolating between $\beta_b A$ and $\beta_b B$ to obtain $\beta_b 2$ in Fig. 2). Note that this extrapolation method means that no compressibility values can be calculated for the first or last confining pressure levels reached in a series of increasing Pc or decreasing Pc tests (e.g. at Pc1 and Pc4 in Fig. 2).

The basic data obtained using the oscillating pore pressure technique on the fault gouge samples in this study are listed in Tables 2–7. A sinusoidal oscillation of the upstream pore pressure generates a downstream oscillation, out-of-phase, and of smaller amplitude but identical frequency. The ratio, r, of downstream-to-upstream amplitudes, and the phase lag, ϕ, are used to calulcate two dimensionless parameters ψ and γ as described in Kranz *et al.* (1990) and Fischer (1992). From these two dimensionless parameters, the permeability, k, and sample storage capacity, β_c, can be easily calculated. Two ways of assessing the experimental errors in permeability and storage capacity measured with this method are by estimating the error in the measurements of r and ϕ, which depend largely on the output sensitivities of the measurement devices, and by statistical variation of repeated oscillation experiment data. In this study, the latter method is used. The lowest permeability measureable depends upon many variables including sample dimensions, downstream reservoir volume, the equilibrium pore pressure, the oscillation frequency and the sensitivity and signal-to-noise ratio of the downstream pore pressure oscillation measurement. The minimum permeability in this study with a minimum oscillating frequency of 0.001 Hz was approximately 3×10^{-21} m^2, but could be lowered if higher pore pressure or a lower downstream reservoir volume were used. Measurements approaching this value are prone to poorer reproducibility than others, hence have higher statistical errors. The maximum permeability measureable was about 3×10^{-14} m^2, using an oscillating frequency of up to 5 Hz, but with many of the higher-frequency oscillation experiments the measured phase lag was smaller than mathematically required to yield the dimensionless parameters ψ and γ. Fortunately, permeability is a function of $\psi^2\gamma$ which can

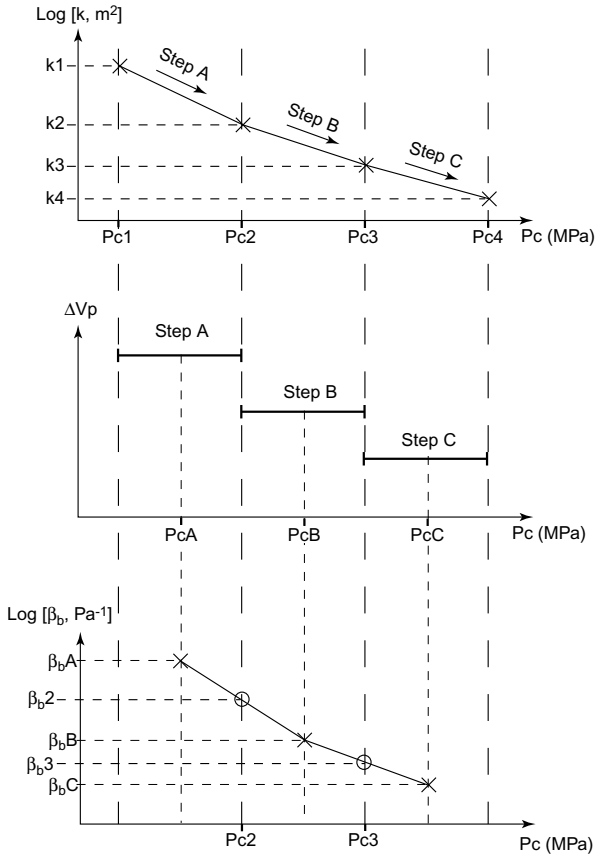

Fig. 2. Illustration of the method used for extrapolating compressibility data measured across intervals of confining pressure steps to equivalent compressibilities at the pressures at the end of the step. Compressibility values determined over finite intervals are assumed to be representative of the compressibility at the mid-point of the interval, i.e. at the median pressure, $(Pc_{start} + Pc_{final})/2$. Compressibilities at the end of pressure steps are estimated by extrapolating between the two adjacent median compressibilities.

Table 2. Data from the oscillating pore pressure experiments for sample Ba.

Exp. No.	Pc (MPa)	Osc. Freq	r	ϕ (rad)	ψ	γ	Log (k, m^2)	Log (β_c, Pa^{-1})
267-01	31.6	2	0.9147	0.283	0.470	—	−14.050	—
		3	0.8999	0.377	0.492	—	−13.914	—
		4	0.947	0.377	0.428	0.56	−13.415	−7.225
		5	0.889	0.942	0.507	—	−13.718	—
267-02	50	2	0.699	0.817	0.248	8.01	−14.399	−8.382
		3	0.5756	0.942	0.843	—	−14.382	—
		4	0.5054	1.131	0.535	2.64	−14.282	−7.899
		5	0.4859	1.571	0.948	—	−14.262	—
267-03	72	1	0.3996	1.037	1.071	—	−15.067	—
		2	0.2623	1.414	0.579	5.13	−14.942	−8.188
		3	0.1932	1.508	0.637	5.89	−14.909	−8.248
		4	0.1798	1.759	1.100	1.86	−14.756	−7.747
267-04	100.3	0.75	0.1558	1.367	1.780	—	−15.633	—
		1	0.1253	1.461	0.217	83.69	−15.603	−9.401
		1.5	0.09305	1.461	2.313	—	−15.559	—
		2	0.07518	1.822	1.007	6.07	−15.495	−8.261
267-05	125.4	0.5	0.08529	1.508	0.260	85.78	−16.072	−9.411
		0.75	0.0625	1.673	0.707	15.54	−16.022	−8.670
		1	0.05339	1.759	0.860	12.18	−15.962	−8.564
267-06	150.3	0.2	0.08778	1.433	2.382	—	−16.363	—
		0.3	0.05899	1.508	2.909	—	−16.457	—
		0.5	0.03774	1.696	0.703	26.31	−16.422	−8.898
267-07	173.6	0.2	0.04316	1.634	0.565	35.78	−16.764	−9.032
		0.25	0.03463	1.696	0.696	29.29	−16.761	−8.945
		0.3	0.03047	1.810	0.905	19.40	−16.731	−8.766
267-08	199.8	0.2	0.01852	1.810	0.883	33.84	−17.127	−9.007
		0.25	0.01564	1.759	0.785	51.10	−17.107	−9.186
		0.3	0.01364	2.073	1.262	21.50	−17.065	−8.811
267-09	197.9	0.2	0.02987	1.659	0.596	46.65	−17.200	−9.422
	$Pp =$	0.25	0.02449	1.759	0.803	31.05	−17.185	−9.245
	30 MPa	0.3	0.01995	1.775	0.823	36.25	−17.195	−9.312
		0.5	0.0109	1.885	0.993	45.19	−17.232	−9.408
267-10	197.5	0.2	0.02004	1.810	0.886	31.04	−17.093	−8.970
		0.25	0.01719	1.822	0.902	34.89	−17.062	−9.021
		0.3	0.01273	1.885	0.996	38.39	−17.111	−9.062
267-11	187.5	0.2	0.02145	1.810	0.888	28.80	−17.062	−8.937
		0.25	0.01474	1.885	1.000	32.87	−17.126	−8.995
		0.3	0.01332	1.810	0.873	48.27	−17.096	−9.162
267-12	198.3	0.2	0.01999	1.759	0.794	39.01	−17.097	−9.069
		0.25	0.01645	1.759	0.787	48.36	−17.086	−9.163
		0.3	0.01333	1.810	0.874	48.16	−17.096	−9.161
267-13	150	0.2	0.02255	1.759	0.799	34.08	−17.044	−9.011
		0.25	0.01648	1.759	0.787	48.26	−17.085	−9.162
		0.3	0.01471	1.659	0.556	109.50	−17.060	−9.517
267-14	150.4	0.2	0.03162	1.634	0.533	55.14	−17.176	−9.494
	$Pp =$	0.25	0.02576	1.634	0.516	72.35	−17.169	−9.612
	30 MPa	0.3	0.02109	1.810	0.888	29.34	−17.169	−9.220
		0.5	0.0131	1.822	0.895	46.69	−17.156	−9.422
267-15	150.5	0.2	0.02182	1.810	0.889	28.26	−17.055	−8.929
		0.25	0.017	1.634	0.490	122.10	−17.076	−9.565
		0.3	0.01599	1.810	0.878	39.68	−17.016	−9.077

Table 2. (continued).

Exp. No.	Pc (MPa)	Osc. Freq	r	ϕ (rad)	ψ	γ	Log (k, m^2)	Log (β_c, Pa^{-1})
267-16	140.6	0.2	0.02098	1.659	0.573	72.16	−17.081	−9.336
		0.25	0.01759	1.822	0.903	34.03	−17.052	−9.010
		0.3	0.01503	1.810	0.876	42.42	−17.043	−9.106
267-17	150.3	0.2	0.0212	1.659	0.573	71.26	−17.075	−9.331
		0.25	0.01776	1.759	0.789	44.46	−17.051	−9.126
		0.3	0.015347	1.659	0.557	104.30	−17.040	−9.496
267-18	100.4	0.2	0.02832	1.684	0.653	40.87	−16.947	−9.089
		0.25	0.02268	1.696	0.669	48.72	−16.948	−9.166
		0.3	0.01781	1.772	0.813	41.69	−16.970	−9.098
		0.5	0.01112	2.199	1.412	20.50	−16.919	−8.790
267-19	91.2	0.2	0.03015	1.659	0.597	46.10	−16.922	−9.142
		0.25	0.02498	1.634	0.514	75.29	−16.908	−9.355
		0.3	0.02015	1.810	0.886	30.85	−16.914	−8.967
		0.5	0.01264	1.885	0.996	38.68	−16.892	−9.066
267-20	100.9	0.2	0.02913	1.608	0.448	84.97	−16.938	−9.407
		0.25	0.0229	1.696	0.669	48.18	−16.943	−9.161
		0.3	0.0197	1.810	0.885	31.63	−16.924	−8.978
		0.5	0.01293	2.011	1.178	26.41	−16.872	−8.900
267-21	100.8	0.2	0.04387	1.583	0.412	66.68	−17.035	−9.577
	$Pp =$	0.25	0.03513	1.602	0.447	70.65	−17.034	−9.602
	30 MPa	0.3	0.02935	1.640	0.545	56.99	−17.033	−9.508
		0.5	0.01742	1.822	0.903	34.39	−17.031	−9.289
267-22	100.8	0.2	0.02924	1.608	0.449	84.50	−16.937	−9.405
		0.25	0.02283	1.696	0.669	48.35	−16.944	−9.162
		0.3	0.0181	1.810	0.882	34.70	−16.961	−9.018
		0.5	0.01139	2.011	1.176	30.17	−16.928	−8.957
267-23	50.2	0.25	0.05109	1.539	0.243	164.89	−16.598	−9.695
		0.3	0.04331	1.621	0.531	40.48	−16.587	−9.085
		0.5	0.02703	1.634	0.520	67.94	−16.572	−9.310
		0.75	0.0175	2.168	1.385	13.48	−16.545	−8.608
267-24	50.6	0.25	0.1061	1.508	0.362	35.41	−16.551	−9.302
	$Pp =$	0.3	0.08596	1.536	0.394	36.97	−16.564	−9.321
	30 MPa	0.5	0.05639	1.602	0.515	33.02	−16.525	−9.272
		0.75	0.03907	1.696	0.706	25.18	−16.505	−9.154
267-25	50.8	0.25	0.05905	1.539	0.288	101.31	−16.534	−9.484
		0.3	0.04915	1.659	0.644	24.07	−16.529	−8.859
		0.5	0.03222	1.728	0.757	26.54	−16.490	−8.902
		0.75	0.02075	1.791	0.854	32.34	−16.505	−8.988
267-26	40.6	0.25	0.07545	1.492	2.571	—	−16.429	—
		0.3	0.06295	1.583	0.477	34.42	−16.424	−9.015
		0.5	0.04142	1.665	0.640	28.98	−16.383	−8.940
		0.75	0.02414	1.885	1.016	19.27	−16.431	−8.763
267-27	50.6	0.25	0.06105	1.539	0.299	91.31	−16.521	−9.439
		0.3	0.05138	1.583	0.439	50.08	−16.515	−9.178
		0.5	0.03178	1.759	0.817	22.98	−16.494	−8.839
		0.75	0.01973	1.885	1.008	24.03	−16.520	−8.859
267-28	30	0.3	0.1542	1.433	0.223	63.88	−16.032	−9.283
		0.5	0.09953	1.524	0.398	31.17	−16.002	−8.972
		0.75	0.07079	1.555	0.408	42.05	−15.977	−9.102
		1	0.05185	1.696	0.734	17.42	−15.980	−8.719

Table 3. Data from the oscillating pore pressure experiments for sample F2xb.

Exp. No.	Pc (MPa)	Osc. Freq	r	ϕ (rad)	ψ	γ	Log (k, m^2)	Log (β_c, Pa^{-1})
256-01	30.2	2	0.1176	1.759	0.981	3.97	−15.107	−8.246
		2.5	0.09426	1.885	1.138	3.61	−15.097	−8.204
		3	0.08918	1.696	0.813	8.04	−15.074	−8.553
256-02	49.9	0.1	0.05422	1.860	1.029	8.15	−16.762	−8.558
		0.2	0.02322	2.011	1.195	14.11	−16.829	−8.797
		0.5	0.006587	2.702	1.946	15.28	−16.889	−8.831
256-03	74.5	0.03	0.008829	3.393	2.656	4.05	−17.805	−8.255
		0.05	0.00451	2.865	2.105	17.77	−18.023	−8.897
256-04	98.1	0.01	0.003455	2.702	1.938	29.68	−18.873	−9.120
		0.01	0.00299	3.016	2.251	21.84	−18.870	−8.986
		0.01	0.002724	2.626	1.860	42.33	−18.991	−9.274
		0.01	0.003189	3.192	2.427	15.95	−18.799	−8.850
		0.01	0.003256	2.890	2.127	23.95	−18.860	−9.026
256-05	124.9	0.003	0.002105	3.121	2.352	26.97	−19.522	−9.078
		0.003	0.002601	3.091	2.324	22.65	−19.436	−9.002
		0.003	0.002477	2.609	1.842	47.83	−19.559	−9.327
		0.003	0.002663	2.955	2.189	26.82	−19.458	−9.076
		0.003	0.002601	3.147	2.385	20.79	−19.421	−8.965
256-06	150.4	0.001	0.002793	3.091	2.325	21.06	−19.882	−8.971
		0.001	0.003296	3.077	2.313	18.12	−19.812	−8.905
		0.001	0.003687	2.850	2.088	22.35	−19.814	−8.997
		0.001	0.003128	3.046	2.281	19.99	−19.843	−8.948
256-07	174	0.001	0.000705	3.212	2.437	71.84	−20.456	−9.503
		0.001	0.000729	4.509	3.734	12.29	−20.060	−8.737
		0.001	0.000428	3.514	2.734	78.66	−20.595	−9.543
		0.001	0.000705	3.197	2.422	73.34	−20.459	−9.512
		0.001	0.000719	4.433	3.657	13.74	−20.090	−8.785
256-08	200	0.001	0.000324	3.845	3.063	66.70	−20.622	−9.471
		0.001	0.000316	4.011	3.228	54.93	−20.583	−9.387
		0.001	0.000271	3.891	3.107	75.20	−20.687	−9.523
		0.001	0.000255	4.102	3.318	60.54	−20.650	−9.429
		0.001	0.000427	4.554	3.775	20.00	−20.281	−8.948
256-09	164.5	0.001	0.000365	4.735	3.956	18.63	−20.290	−8.917
		0.001	0.000341	4.780	4.001	18.82	−20.305	−8.922
		0.001	0.000315	4.026	3.244	53.94	−20.580	−9.379
		0.001	0.000446	4.222	3.441	29.39	−20.367	−9.115
256-10	50.5	0.001	0.001986	3.121	2.352	28.61	−20.025	−9.104
		0.001	0.002207	2.971	2.039	40.79	−20.055	−9.258
		0.001	0.002207	2.789	2.023	41.20	−20.053	−9.262
256-11	30.4	0.005	0.001099	2.978	2.208	63.62	−19.773	−9.724
		0.005	0.00088	2.695	1.926	119.50	−19.570	−9.367
		0.005	0.001168	3.072	2.301	52.42	−19.882	−9.896
		0.005	0.000723	2.564	1.791	177.50	−19.618	−9.451
256-12	25.4	0.005	0.0045	2.601	1.838	26.36	−19.076	−9.068
		0.005	0.004583	2.469	1.701	31.81	−19.091	−9.150
		0.005	0.00525	2.827	2.069	16.05	−18.964	−8.853
		0.005	0.004917	2.394	1.620	33.50	−19.071	−9.172
		0.005	0.00525	2.865	2.107	15.19	−18.955	−8.829

Table 4. Data from the oscillating pore pressure experiments for sample F3xa.

Exp. No.	Pc (MPa)	Osc. Freq	r	ϕ (rad)	ψ	γ	Log (k, m^2)	Log (β_c, Pa^{-1})
238-01	30.4	1.5	0.275	1.367	0.478	7.31	−14.833	−8.561
		2	0.2172	1.508	0.698	4.25	−14.801	−8.326
		2.5	0.1766	1.571	0.743	4.68	−14.800	−8.367
		3	0.1607	1.649	0.868	3.69	−14.753	−8.264
238-02	50	0.3	0.1136	1.583	0.621	10.98	−15.936	−8.738
		0.5	0.08241	1.948	1.209	3.63	−15.812	−8.257
		0.7	0.05556	2.066	1.323	4.50	−15.837	−8.350
238-03	74.2	0.1	0.05794	1.659	0.665	19.06	−16.712	−8.978
		0.2	0.02688	2.035	1.234	11.31	−16.721	−8.751
		0.3	0.01813	2.450	1.707	7.75	−16.663	−8.586
238-04	100.7	0.05	0.02428	1.973	1.145	14.81	−17.375	−8.867
		0.1	0.01113	2.538	1.787	11.34	−17.345	−8.752
238-05	126	0.03	0.01717	2.054	1.243	17.60	−17.744	−8.943
		0.03	0.01698	1.998	1.168	20.41	−17.754	−9.007
		0.03	0.01717	2.018	1.194	19.22	−17.747	−8.981
		0.03	0.01736	1.960	1.115	22.06	−17.747	−9.041
		0.03	0.01755	1.998	1.169	19.70	−17.739	−8.992
238-06	150.8	0.015	0.01444	1.998	1.164	24.24	−18.126	−9.082
		0.015	0.01367	2.093	1.286	20.55	−18.141	−9.010
		0.015	0.0135	2.149	1.355	18.48	−18.141	−8.964
		0.015	0.0141	2.018	1.189	23.69	−18.135	−9.072
		0.015	0.01435	1.998	1.164	24.41	−18.129	−9.085
238-07	174.6	0.01	0.0161	1.810	0.879	39.34	−18.269	−9.292
		0.01	0.01673	1.810	0.880	37.74	−18.252	−9.274
		0.01	0.01555	1.709	0.680	68.90	−18.289	−9.536
		0.01	0.01427	1.909	1.036	31.48	−18.315	−9.195

be found from the approximation $\psi^2\gamma = 0.5(r^{-2} - 1)^{0.5}$ over a limited range of ψ, γ. However, storage capacity can not be determined in such cases. In Tables 2–7, where these cases occur, the $\psi^2\gamma$ value is shown in the ψ column, and the γ column is marked with a '—'.

4. Results

Firstly, data on length and volume changes during confining pressure changes are presented in the form of strains. Length strains of the sample axes are calculated from the length changes measured using the piston hitpoint method. Figure 3(a) shows that axial strains measured in this way vary very little among the different gouge samples, from 5.2 to 6.2% shortening at Pc = 200 MPa. In each case, the sample did not recover its initial length upon deconfinement, and the data in Fig. 3(a) show significant permanent shortening with less than 50% recovery from peak strain. Volumetric strains were calculated by dividing the measured pore volume changes by initial total sample volume. This is not equivalent to pore volume strain, although related, because initial porosity could not be measured. With the assumption that the compressibility of the component minerals is negligible in comparison to that of the sample as a whole, these pore volume changes can also be used to calculate sample bulk compressibility (β_b). The volume strain data in Fig. 3(b) show a systematic trend between the amount of volume strain at any given pressure, and the location and grain size of the sample. The finest-grained gouge from the central slip zone (F2) shows the lowest volume strain whilst the coarsest gouge from close to the edge of the fault zone (F8) shows the highest volume strain. Bulk compressibilities calculated from these data (Fig. 4) show a drop of half an order of magnitude at the onset of Pc decrease, due to the fact that much of the volumetric strain during confinement is permanent, plastic strain. Compressibility data vary very little among the samples (Fig. 4) except towards the peak of the increasing Pc path where compressibility in the coarser gouges increases, probably due to the onset of intraclast fracturing (Zhu and Wong, 1997). Indeed there seems to be a correlation between the distance of the gouge sample from the central slip zone (related to clast size and proportion), and both the compressibility at high pressure and the onset of rising compressibility. This suggests that coarse gouges become increasingly susceptible to intraclast fracturing as they become closer to clast-supported framework materials at high pressure.

The axial strain can be used to calculate the theoretical isotropic volumetric strain, for comparison with the actual

Table 5. Data from the oscillating pore pressure experiments for sample F4xb.

Exp. No.	Pc (MPa)	Osc. Freq	r	ϕ (rad)	ψ	γ	Log (k, m^2)	Log (β_c, Pa^{-1})
237-01	30.8	1	0.4784	1.100	0.290	10.58	−14.688	−8.748
		2.5	0.2632	1.335	0.305	19.38	−14.596	−9.011
		3	0.2175	1.508	0.698	4.24	−14.576	−8.351
237-02	50	0.3	0.06181	1.734	0.830	11.28	−16.152	−8.776
		0.5	0.04174	1.948	1.139	8.58	−16.086	−8.657
		0.7	0.02955	2.023	1.222	10.48	−16.088	−8.744
237-03	74.8	0.1	0.02594	1.986	1.166	13.30	−16.996	−8.848
		0.2	0.01114	2.412	1.652	13.93	−17.017	−8.868
		0.3	0.005373	2.714	1.955	18.53	−17.111	−8.992
237-04	98.5	0.05	0.01404	2.262	1.490	14.21	−17.538	−8.876
		0.1	0.006345	2.199	1.404	36.58	−17.596	−9.287
237-05	125.5	0.03	0.006527	2.149	1.344	39.31	−18.112	−9.318
		0.03	0.006785	2.187	1.390	34.97	−18.091	−9.267
		0.03	0.00685	2.073	1.251	43.97	−18.099	−9.367
		0.03	0.006994	2.412	1.644	22.90	−18.053	−9.084
		0.03	0.006721	2.450	1.685	22.13	−18.059	−9.069
237-06	150.5	0.02	0.00781	1.909	1.025	59.10	−18.230	−9.495
		0.02	0.008014	1.659	0.537	215.60	−18.231	−10.057
		0.02	0.00747	1.759	0.768	112.20	−18.258	−9.774
		0.02	0.008149	1.608	0.371	445.30	−18.225	−10.372
		0.02	0.008217	1.810	0.864	80.25	−18.215	−9.628
237-07	175.3	0.02	0.001938	2.463	1.689	77.01	−18.779	−9.610
		0.02	0.002145	2.161	1.351	118.70	−18.773	−9.798
		0.02	0.002076	2.112	1.292	135.80	−18.793	−9.857
		0.02	0.002145	1.759	0.757	403.00	−18.801	−10.329
		0.02	0.002491	1.960	1.091	163.30	−18.726	−9.937
237-08	200.5	0.01	0.01301	1.709	0.674	83.86	−18.319	−9.647
		0.02	0.002129	1.810	0.853	318.80	−18.803	−10.227

measured volumetric strain (Fig. 3(c)). The data show a reasonably strong 1:1 relationship for the coarser samples F8 and F5, but an increasingly poor correlation for samples that are progressively finer-grained and closer to the central slip zone, with sample F2 showing the biggest mismatch. The most likely reason for this is that this is due to the increasing anisotropy of compressibility with decreasing gouge grain size.

In order to examine the effect of permanent compaction on properties subsequent to compaction more closely, a further experiment on a fresh sample of foliated gouge (F3xb) was performed in which three complete cycles of confining pressure were made. Figure 5 shows that after the first pressure cycle peak, later pressure cycling has only very small to negligible permanent effects. Hence the sample can be considered to deform elastically thereafter, provided that later $Pc - Pp$ does not exceed this previous peak. This is also manifested in the compressibility data from this experiment (Fig. 5(c)) which show relatively consistent values for later pressure cycles along with the deconfining portion of the first pressure cycle. The consistency in values for later pressure cycles, both during increasing and decreasing Pc, indicates elastic behaviour. The fact that compressibility is not constant means that the sample is behaving in a non-linear elastic manner. The higher compressibility values for the confining part of the first Pc cycle therefore reflect the additional input of plastic deformation during initial compaction. An interesting effect of hysteresis is shown (Figs. 5(a), (b)), noticed previously in fracture contact experiments (e.g. Scholz and Hickman, 1983) and evident in permeability measurements during pressure cycling (e.g. Morrow *et al.*, 1986). Such hysteresis is reflected in anomalously low values for the first compressibility measurement in a series of increasing Pc or decreasing Pc steps.

Permeability data (Fig. 6(a)) show a large variation among the different samples, with the gouge from the central slip zone (F2) having a much lower permeability than the other samples. Of the F-series gouges, the coarsest (F8) has the highest permeability, although the coarse white gouge (Ba) derived from Ryoke cataclasites on the other side of the fault core has an even higher permeability. The samples show 3 to 5 orders of magnitude permeability reduction as

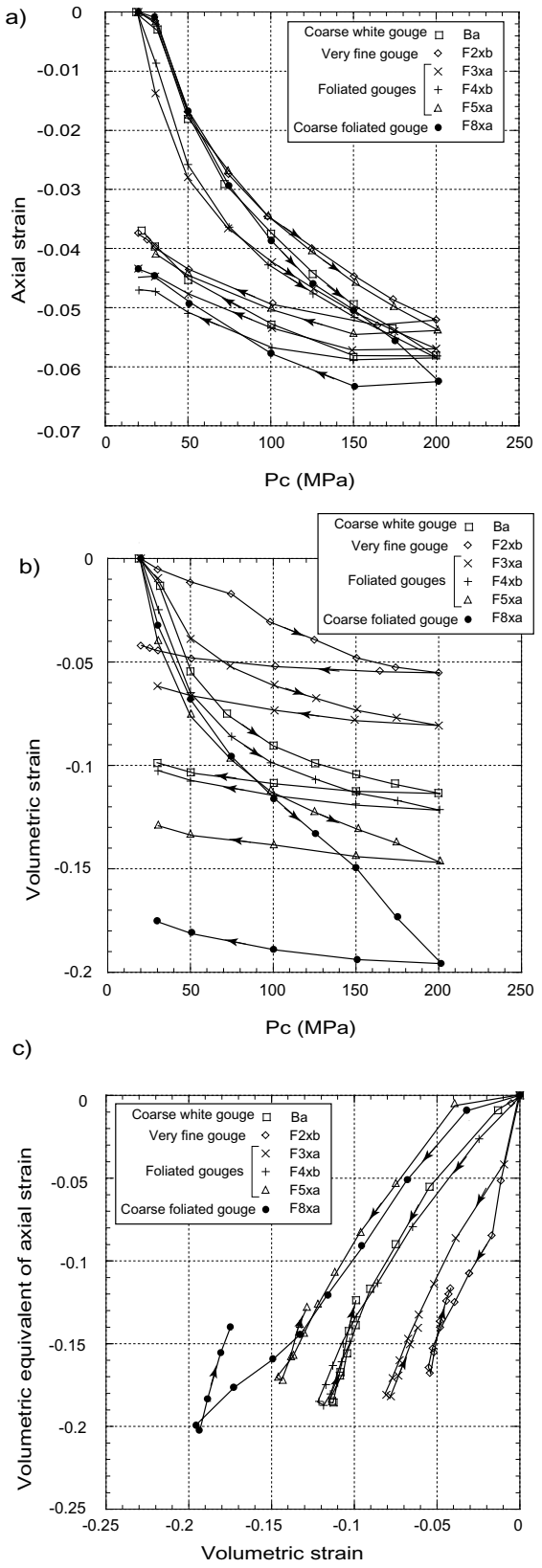

Fig. 3. The relationship between strain and confining pressure (Pc) at a constant nitrogen gas pore pressure of 20 MPa for the gouge samples studied. (a) Axial strain estimated from piston hitpoint data after each pressure increase. (b) Volumetric strain data measured from pore volume changes during confining pressure increases at constant pore pressure. (c) Comparison of volumetric strain calculated from the axial strain data by assuming isotropic behaviour versus the measured volumetric strain.

confining pressure is increased up to 200 MPa. In each case the pressure sensitivity of permeability decreases as pressure (compaction) increases. This is most obvious for the very fine gouge (sample F2) from the central slip zone which has very high pressure sensitivities in the early stages, possibly due to the repair of cracks and foliation partings induced by artificial sample damage (Wibberley and Shimamoto, 2003).

A full description of hydrodynamic properties includes the hydraulic diffusivity (D_h), which is related to the permeability (k) and storage capacity per unit sample volume (β_c) in the following way:

$$D_h = \frac{k}{\eta \beta_c} \tag{1}$$

where η is the fluid viscosity. Storage capacity is defined as the change in the volume of pore fluid held in the system due to a unit fluid pressure change, and was measured along with permeability using nitrogen as a pore fluid. In poroelasticity theory, storage capacity is related to porosity (n) and the compressibilities of the fluid (β_f), mineral grain (β_s) and sample bulk framework (β_b) by the following relationship, assuming that an equal change in both confining and pore pressures (i.e. zero change in $Pc - Pp$) results in no porosity change:

$$\beta_c = n(\beta_f - \beta_s) + (\beta_b - \beta_s). \tag{2}$$

The measured storage capacity is partly a reflection on fluid compressibility. In order to correct our measurements for the case of water storage, we firstly calculate the theoretical porosity from the measurements of storage capacity as in Eq. (2). It must be stressed that the use of Eq. (2) assumes that all constituent minerals have the same compressibility (β_s), which may not strictly be true for rocks containing both quartz and phyllosilicates (Green and Wang, 1986). Published nitrogen compressibility (β_f) data (at room temperature and $Pp = 20$ MPa, $\beta_f = 4.32 \times 10^{-8}$ Pa^{-1}), a value of 1.2×10^{-11} Pa^{-1} for compressibility of mica (β_s) independent of pressure (Birch, 1966) and the bulk framework compressibility data (β_b) (Fig. 3) are used. Porosities calculated in this way are in the order of 5–10% at low pressure, decreasing to 0.1–1.5% at high confining pressure. Ongoing work is being carried out to adapt the gas rig for direct porosity measurements for comparison. Storage capacity of the sample in a gouge-water system is then calculated simply from Eq. (2) with the appropriate water compressibility data and the values of β_s and β_b used previously. From this and the permeability data (Fig. 6(a)), hydraulic diffusivities are calculated using Eq. (1) with the room temperature viscosity of water (Fig. 6(b)). The variation in hydraulic diffusivity among the samples is similar to that of permeability because compressibility does not vary much among the samples. However, unlike the permeability, the hydraulic diffusivities remain constant or even decrease along the decreasing Pc path (Fig. 6(b)), because of the increase in measured compressibility as confining pressure decreases. The drop of half an order of magnitude in compressibility at the onset of decreasing Pc causes the calculated hydraulic diffusivity to be higher than at the end of the increasing Pc path. This is thought to be because the measured compressibility contains

Table 6. Data from the oscillating pore pressure experiments for sample F5xa.

Exp. No.	Pc (MPa)	Osc. Freq	r	ϕ (rad)	ψ	γ	Log (k, m^2)	Log (β_c, Pa^{-1})
236-01	30.5	1	0.77766	0.534	0.636	—	−14.452	—
		2	0.4	0.754	1.070	—	−14.603	—
		3	0.5	0.942	0.931	—	−14.306	—
		4	0.488	1.005	0.946	—	−14.195	—
236-02	50.4	1	0.1668	1.508	0.566	8.87	−15.299	−8.627
		1.5	0.13	1.461	0.566	14.37	−15.248	−9.470
		2	0.1053	1.571	0.585	17.47	−15.207	−8.837
		3	0.0815	1.602	0.248	61.76	−17.144	−8.922
236-03	74.2	0.3	0.08748	1.527	0.362	43.00	−16.119	−9.313
		0.5	0.0511	1.822	0.964	10.00	−16.114	−8.679
		1	0.0297	2.168	1.406	7.54	−16.019	−8.557
236-04	98.7	0.1	0.06087	1.634	0.612	21.49	−16.751	−9.011
		0.2	0.03008	1.759	0.814	24.51	−16.754	−9.068
236-05	125	0.1	0.01466	1.810	0.876	43.57	−17.349	−9.120
		0.1	0.01654	1.960	1.115	23.21	−17.372	−9.143
		0.1	0.01504	2.061	1.248	19.96	−17.338	−8.979
		0.1	0.01429	1.935	1.075	29.10	−17.305	−9.045
		0.1	0.01504	1.935	1.076	27.57	−17.369	−9.318
236-06	151.5	0.05	0.009237	2.011	1.172	37.52	−17.858	−9.253
		0.05	0.009839	2.262	1.483	20.64	−17.803	−8.994
		0.05	0.01004	2.187	1.395	23.34	−17.803	−9.047
		0.05	0.009839	2.111	1.303	27.84	−17.820	−9.124
		0.05	0.01004	2.237	1.454	21.18	−17.797	−9.005
236-07	174.6	0.03	0.00696	2.809	2.055	12.30	−18.083	−8.769
		0.03	0.0068	2.394	1.624	24.01	−18.169	−9.060
		0.03	0.00736	2.620	1.864	15.41	−18.097	−8.867
		0.03	0.00696	2.507	1.745	19.49	−18.141	−8.969
		0.03	0.00752	2.507	1.746	17.98	−18.107	−8.934
236-08	200.9	0.02	0.004502	2.262	1.474	46.14	−18.545	−9.343
		0.02	0.004	2.036	1.197	83.14	−18.620	−9.599
		0.02	0.004502	2.312	1.530	42.16	−18.538	−9.304
		0.02	0.004589	2.161	1.356	54.88	−18.548	−9.419
		0.02	0.004848	2.388	1.614	34.34	−18.496	−9.215
236-09	200.2	0.02	0.006463	1.960	1.097	61.93	−18.648	−9.703
	$Pp =$	0.02	0.006822	2.136	1.329	38.53	−18.609	−9.497
	30 MPa	0.02	0.006535	2.136	1.329	40.27	−18.628	−9.516
		0.02	0.006463	2.111	1.298	42.95	−18.635	−9.544
		0.02	0.00632	2.136	1.329	41.67	−18.643	−9.531
236-10	190.1	0.02	0.005727	2.337	1.560	31.55	−18.429	−9.135
		0.02	0.004772	1.935	1.059	90.62	−18.551	−9.594
		0.02	0.004599	2.237	1.445	47.30	−18.539	−9.311
		0.02	0.004165	2.111	1.294	67.25	−18.596	−9.464
		0.02	0.004859	2.413	1.641	32.86	−18.491	−9.153
236-11	200.4	0.02	0.004359	2.438	1.667	35.20	−18.534	−9.226
		0.02	0.004017	2.463	1.694	36.68	−18.566	−9.244
		0.02	0.004872	2.286	1.502	40.72	−18.507	−9.289
		0.02	0.003846	2.337	1.557	47.40	−18.604	−9.355
		0.02	0.004957	2.363	1.587	34.99	−18.489	−9.223

Table 6. (continued).

Exp. No.	Pc (MPa)	Osc. Freq	r	ϕ (rad)	ψ	γ	Log (k, m^2)	Log (β_c, Pa^{-1})
236-12	150	0.02	0.004026	2.187	1.386	59.59	−18.603	−9.454
		0.02	0.00454	2.161	1.355	55.56	−18.553	−9.424
		0.02	0.004454	2.011	1.164	79.28	−18.575	−9.578
		0.02	0.004111	1.909	1.019	114.00	−18.617	−9.736
		0.02	0.004454	2.262	1.474	46.65	−18.550	−9.348
236-13	100.4	0.03	0.00623	1.885	0.985	80.67	−18.261	−9.586
		0.03	0.005902	2.150	1.345	43.43	−18.263	−9.317
		0.03	0.004672	2.112	1.296	59.75	−18.369	−9.455
		0.03	0.00582	1.923	1.043	76.63	−18.289	−9.564
		0.03	0.006967	1.960	1.098	57.33	−18.207	−9.438
236-14	100.8	0.03	0.008377	1.847	0.927	67.98	−18.366	−9.744
	$Pp =$	0.03	0.008333	1.810	0.864	78.97	−18.370	−9.809
	30 MPa	0.03	0.009167	1.923	1.049	47.98	−18.322	−9.592
		0.03	0.009123	2.035	1.205	35.79	−18.316	−9.465
		0.03	0.009002	1.885	0.990	55.17	−18.333	−9.653
236-15	101	0.03	0.005503	1.847	0.922	104.90	−18.318	−9.700
		0.03	0.005585	2.073	1.249	54.20	−18.295	−9.413
		0.03	0.005339	1.923	1.042	83.70	−18.326	−9.602
		0.03	0.004271	1.923	1.040	905.10	−18.424	−9.701
		0.03	0.00501	2.187	1.387	47.70	−18.330	−9.358
236-16	90.5	0.03	0.005082	2.112	1.296	54.84	−18.332	−9.418
		0.03	0.004836	2.187	1.387	49.45	−18.346	−9.373
		0.03	0.004344	2.450	1.680	34.64	−18.358	−9.219
		0.03	0.004426	2.412	1.639	36.19	−18.356	−9.238
		0.03	0.004918	2.375	1.601	34.55	−18.315	−9.218
236-17	99.9	0.03	0.004124	2.337	1.557	44.15	−18.397	−9.324
		0.03	0.004124	2.601	1.836	28.85	−18.356	−9.139
		0.03	0.004784	2.375	1.600	35.54	−18.327	−9.230
		0.03	0.004619	2.035	1.197	71.95	−18.381	−9.536
		0.03	0.004836	2.262	1.474	42.89	−18.337	−9.311
236-18	50	0.05	0.007026	2.231	1.442	31.02	−17.955	−9.171
		0.05	0.006707	2.262	1.477	30.69	−17.972	−9.166
		0.05	0.005828	2.011	1.167	60.26	−18.060	−9.459
		0.05	0.006547	2.168	1.367	37.69	−17.994	−9.255
		0.05	0.007585	2.356	1.584	22.87	−17.905	−9.038
236-19	50.3	0.05	0.0163	1.854	0.953	32.86	−17.853	−9.428
	$Pp =$	0.05	0.01663	2.011	1.184	20.23	−17.831	−9.217
	30 MPa	0.05	0.01608	1.932	1.073	25.91	−17.853	−9.325
		0.05	0.01552	1.932	1.072	26.91	−17.868	−9.341
		0.05	0.01563	1.932	1.072	26.70	−17.865	−9.338
236-20	40.1	0.05	0.01153	1.916	1.042	38.58	−17.768	−9.266
		0.05	0.01075	2.231	1.448	19.96	−17.768	−8.979
		0.05	0.01083	2.042	1.217	29.45	−17.786	−9.148
		0.05	0.0113	2.356	1.591	15.09	−17.728	−8.858
		0.05	0.01184	2.073	1.259	24.95	−17.743	−9.076
236-21	30.5	0.1	0.01464	2.011	1.181	23.17	−17.354	−9.044
		0.1	0.01368	1.979	1.136	26.98	−17.387	−9.110
		0.1	0.01329	2.105	1.301	20.61	−17.388	−8.993
		0.1	0.01349	2.042	1.221	23.40	−17.388	−9.048
		0.1	0.01291	2.105	1.300	21.25	−17.400	−9.007

Table 7. Data from the oscillating pore pressure experiments for sample F8xa.

Exp. No.	Pc (MPa)	Osc. Freq	r	ϕ (rad)	ψ	γ	Log (k, m^2)	Log (β_c, Pa^{-1})
251-01	30.25	3	0.8	0.283	0.612	—	−14.154	—
		3.5	0.697	0.880	0.717	—	−14.225	—
		4	0.6627	0.754	0.752	—	−14.208	—
		5	0.6071	0.628	0.809	—	−14.175	—
251-02	50.1	3	0.256	1.319	1.374	—	−14.857	—
		4	0.2303	1.382	0.365	15.53	−14.829	−8.667
		5	0.1973	1.885	1.338	0.97	−14.694	−7.461
251-03	74.6	2	0.0542	1.759	0.861	11.94	−15.704	−8.553
		2.5	0.05322	1.963	1.180	6.14	−15.592	−8.264
		3	0.05739	1.979	1.209	5.36	−15.475	−8.205
251-04	100.3	0.5	0.04939	1.696	0.729	18.59	−16.354	−8.745
		0.7	0.03736	1.671	0.645	31.66	−16.332	−8.977
		1	0.02437	2.011	1.197	13.38	−16.340	−8.603
251-05	125.4	0.2	0.03867	1.634	0.553	41.80	−16.863	−9.097
		0.3	0.02534	1.810	0.896	23.92	−16.864	−8.855
		0.5	0.01672	2.199	1.421	13.30	−16.788	−8.600
251-06	149.9	0.1	0.0326	1.734	0.770	25.30	−17.234	−8.879
		0.2	0.0156	1.885	1.001	30.94	−17.248	−8.967
		0.3	0.01035	2.262	1.484	19.58	−17.215	−8.768
251-07	175	0.1	0.01543	1.979	1.139	23.76	−17.547	−8.852
		0.1	0.01472	2.011	1.181	23.03	−17.565	−8.838
		0.1	0.01517	1.885	1.001	31.88	−17.562	−8.980
		0.1	0.01613	1.759	0.786	49.40	−17.542	−9.170
		0.1	0.01613	2.073	1.266	18.01	−17.518	−8.732
251-08	200.2	0.1	0.005718	2.199	1.403	40.69	−17.961	−9.086
		0.15	0.00367	2.262	1.472	56.80	−17.972	−9.230
251-09	200.5	0.15	0.006281	2.215	1.422	35.86	−18.017	−9.305
	$Pp =$	0.15	0.007017	2.168	1.368	35.10	−17.974	−9.296
	30 MPa	0.15	0.00687	2.121	1.310	39.54	−17.988	−9.348
		0.15	0.00633	2.262	1.477	32.56	−18.008	−9.263
		0.15	0.006232	2.215	1.422	36.15	−18.020	−9.309
251-10	190.5	0.1	0.006127	2.199	1.404	37.91	−17.931	−9.055
		0.15	0.003368	2.356	1.577	52.48	−17.997	−9.196
251-11	150.7	0.1	0.00617	2.199	1.404	37.64	−17.928	−9.052
		0.1	0.006655	2.199	1.404	34.83	−17.894	−9.018
		0.1	0.005754	2.231	1.440	38.07	−17.955	−9.057
		0.1	0.00617	2.199	1.404	37.64	−17.928	−9.052
		0.1	0.006239	2.325	1.547	29.53	−17.907	−8.946
251-12	100.1	0.1	0.008243	2.011	1.170	42.20	−17.820	−9.101
		0.1	0.008243	2.199	1.407	27.94	−17.801	−8.922
		0.1	0.008639	2.011	1.171	40.21	−17.799	−9.080
		0.1	0.008375	2.073	1.253	35.75	−17.807	−9.029
		0.1	0.008507	2.011	1.171	40.85	−17.806	−9.087

Table 7. (continued).

Exp. No.	Pc (MPa)	Osc. Freq	r	ϕ (rad)	ψ	γ	Log (k, m^2)	Log (β_c, Pa^{-1})
251-13	100.5	0.15	0.008594	2.032	1.199	38.39	−17.898	−9.335
	$Pp =$	0.15	0.00889	1.960	1.102	44.54	−17.889	−9.400
	30 MPa	0.15	0.01128	2.111	1.306	24.14	−17.771	−9.134
		0.15	0.008756	2.073	1.254	34.14	−17.886	−9.284
		0.15	0.008504	1.998	1.154	42.10	−17.905	−9.375
251-14	100.7	0.1	0.007722	2.011	1.170	45.14	−17.849	−9.131
		0.1	0.007925	1.948	1.082	51.95	−17.842	−9.192
		0.1	0.008128	1.948	1.083	50.62	−17.832	−9.180
		0.1	0.008061	2.073	1.253	37.19	−17.824	−9.046
		0.1	0.008196	2.136	1.332	31.89	−17.811	−8.980
251-15	90.4	0.1	0.009636	2.073	1.255	30.92	−17.745	−8.966
		0.1	0.009636	2.262	1.482	21.09	−17.724	−8.800
		0.1	0.009332	2.136	1.333	27.89	−17.753	−8.922
		0.1	0.009467	2.073	1.255	31.49	−17.753	−8.974
		0.1	0.008723	2.011	1.171	39.81	−17.795	−9.076
251-16	100.1	0.1	0.008641	2.388	1.621	18.93	−17.754	−8.753
		0.1	0.007966	2.450	1.687	18.56	−17.781	−8.745
		0.1	0.008708	2.388	1.621	18.78	−17.751	−8.750
		0.1	0.008033	2.262	1.480	25.48	−17.804	−8.882
		0.1	0.008236	2.011	1.170	42.24	−17.820	−9.102
251-17	50.6	0.15	0.01349	1.744	0.749	65.19	−17.445	−9.290
		0.15	0.01391	1.649	0.527	128.80	−17.435	−9.586
		0.15	0.01433	1.744	0.751	61.05	−17.419	−9.262
		0.15	0.01475	1.744	0.752	59.16	−17.406	−9.248
		0.15	0.01293	1.885	0.997	37.76	−17.456	−9.053
251-18	40.2	0.15	0.0244	1.696	0.673	44.72	−17.188	−9.127
		0.2	0.01822	2.011	1.187	18.35	−17.169	−8.740
251-19	29.7	0.5	0.01818	2.011	1.187	18.39	−16.772	−8.741
		0.5	0.01818	2.073	1.269	15.84	−16.765	−8.676
		0.5	0.01955	2.136	1.350	12.77	−16.726	−8.582
		0.5	0.01909	2.136	1.350	13.10	−16.737	−8.593
		0.5	0.01727	2.011	1.185	19.43	−16.795	−8.764

a significant plastic component as Pc increases to a peak for the first time, but behaves elastically after the peak (see discussion in Subsection 5.1). The hydraulic diffusivity values calculated for the decreasing Pc paths are therefore thought to be closer to representing true poro-elastic hydraulic diffusivities. It should be noted that the values of permeability and hydraulic diffusivity on the deconfining path will be dependent on the peak value of confining pressure experienced by the sample (Zhang and Cox, 2000; Wibberley and Shimamoto, 2003). A fault gouge subjected to a lower confining pressure (at the same pore fluid pressure) will not compact as much and therefore will exhibit higher permeabilities and hydraulic diffusivities during deconfinement than a sample subjected to a higher peak confining pressure.

5. Discussion and Implications for Slip Processes

5.1 Applicability of the measurements to hydraulic diffusivity of gouge-water systems

Two problems with applying the measurements presented in this paper to estimate the hydraulic diffusivity of fault gouge are the effect on measured gouge permeability of using nitrogen gas rather than water, and the use of the compressibility data obtained over finite strain intervals to estimate the elastic pore strain compressibility. Klinkenberg (1941) found that using different gases as pore fluids resulted in different permeabilities, whereas using different liquids did not. This 'Klinkenberg effect' was ascribed to a phenomenon of loss of continuity between pore walls and the adjacent gas molecules, unlike for liquids which are stationary at the walls. Using gas permeability will result in

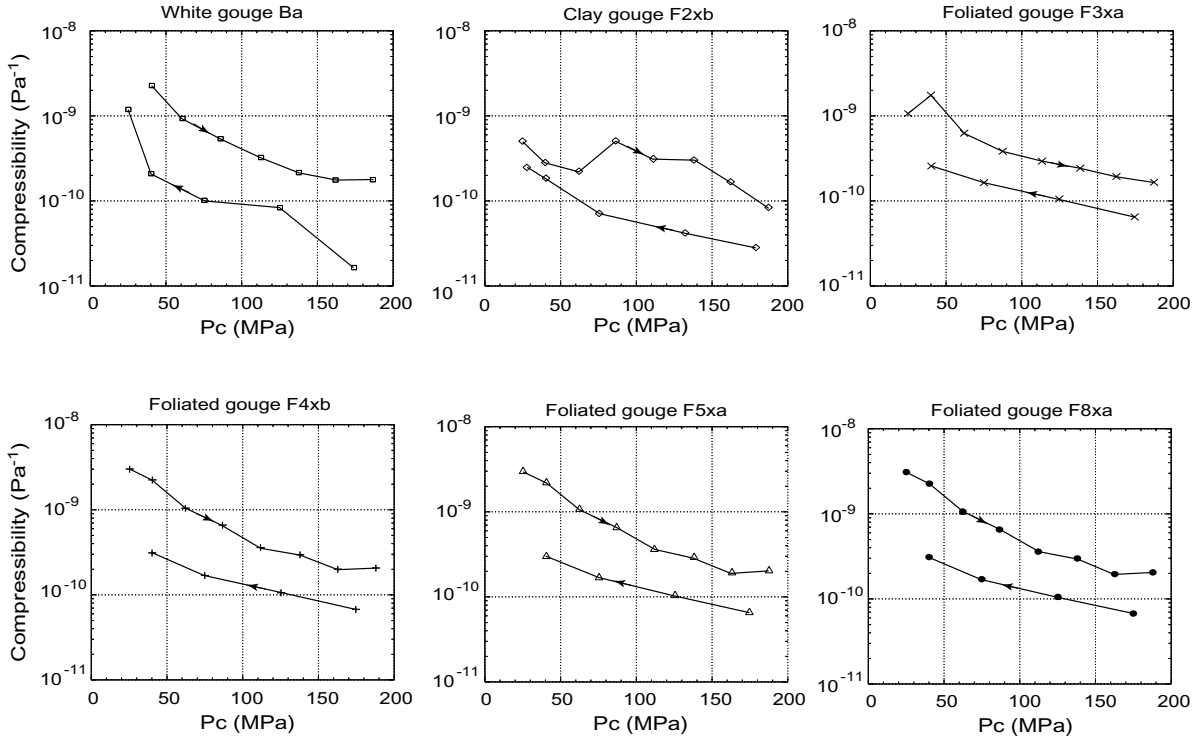

Fig. 4. Bulk framework compressibility data for each of the gouge samples studied.

higher flow rates than predicted by Darcy's law and therefore provide an overestimate of the permeability of a porous medium with water as the pore fluid. A calculation for the case of nitrogen at a pore pressure of 20 MPa has shown that the Klinkenberg effect will lead to this overestimate being less than 10% (Wibberley and Shimamoto, 2003). Nevertheless, comparing permeability measurements on naturally dry non-swelling clay gouges (illite/muscovite) using argon gas and water showed that water permeability is typically one order of magnitude lower than gas permeability (Faulkner and Rutter, 2000). After reviewing possible permeability-reducing mechanisms for the case of water, Faulkner and Rutter (2000) suggested that structured water adsorbed on to the surface of the clay minerals could reduce the pore throat apertures sufficiently to cause the observed permeability reduction. The Median Tectonic Line gouge samples must have been saturated with water *in situ*, and drying the gouge at 80°C prior to the experiments was intended to eliminate the free pore water but not the adsorbed water on the clay mineral surfaces. Although it is difficult to check this, it is assumed that the permeability data reported here are comparable to the permeability of a water-saturated clay gouge, because a water-saturated clay gouge will also have such adsorbed water. An interesting point to be made here is that the coarser gouges, which exhibited higher permeabilities than the finer gouges (Fig. 6(a)), are also the clay-poor gouges and contain higher proportions of quartz microclasts. Thus although the impact of grain size on measured permeability is likely to be important, the effect of mineralogy should also be taken into account due to the preference of this structured water for clay minerals.

The calculations of hydraulic diffusivity also rely on a valid application of the compressibility data to the water-saturated gouge pore storage system. The compressibility of the gas-saturated gouge was measured over finite strain intervals, corresponding to confining pressure steps of typically 25 MPa or more. During the first confining pressure cycle, increasing confining pressure led to both an elastic (recoverable) and a plastic (irrecoverable) component to the volumetric strain as demonstrated by the resulting permanent strain at the end of the pressure cycle (Fig. 3). Thus the calculated compressibility, related to the finite strain, will be significantly higher than the elastic compressibility. In elastic-plastic theory of soil mechanics based on experimental data (e.g. Wood, 1990), a clay or sand aggregate deforms elastically initially upon loading, but reaches a yield point beyond which plastic deformation occurs. If the load is totally removed somewhere beyond the yield point, elastic recovery occurs so that the remaining strain is the plastic component. Upon re-loading, the sample will deform elastically up to the previous peak stress state (which will act as the new yield point), and then plastically beyond this point. The yield point of the gouges was probably initially very low, but after confinement the new yield point will have been at a pressure ($Pc - Pp$) of 180 MPa, because this was the peak pressure to which each gouge sample was subjected. Hence all the compressibilities calculated for the confining part of the first pressure cycle will result from both elastic and plastic components of strain, whereas those calculated for the deconfining part will be elastic compressibilities only. This explains why the compressibilities measured during deconfinement are approximately half an order-of-magnitude lower than during initial confinement—the difference being the plastic component of strain in the compressibility calculation. A check on the later behaviour was made by pressure cycling over three cycles (Fig. 5). The compressibility data

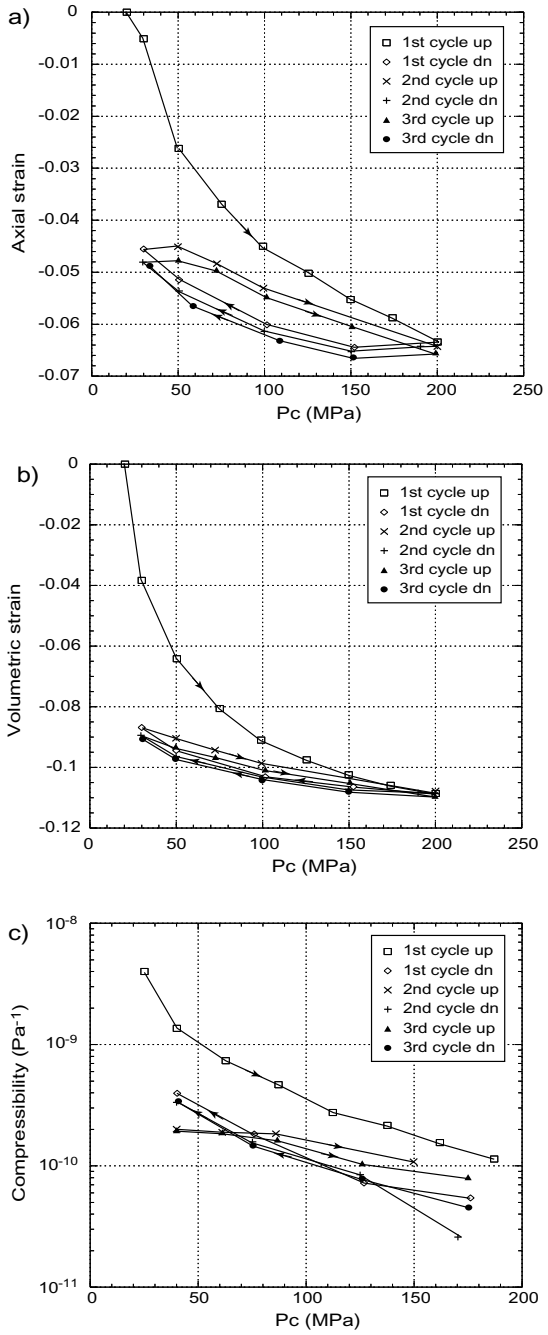

Fig. 5. Poroelastic data for foliated gouge sample F3xb. Each pressure cycle produced close to 100% recovery of strain except for the first cycle. Hence behaviour is elastic, after compaction to the first Pc peak. (a) Axial strain data. (b) Volumetric strain data. (c) Bulk framework compressibility data. Note the effect that hysteresis has on the first compressibility measurement at the start of a new increasing Pc or decreasing Pc path.

(Fig. 5(c)) were found to be consistent from cycle to cycle, and independent of whether the path was of increasing Pc or decreasing Pc. This repeat behaviour indicates elasticity, but the fact that compressibility is still dependent upon pressure demonstrates that the sample behaviour is non-linearly elastic. This is important for the translation of the gouge 'bulk' or 'matrix' compressibility into the calculation of hydraulic diffusivity for the case of a water-saturated gouge, because such a calculation is valid only for poro-elastic behaviour. Indeed, the oscillating pore pressure experiments used to determine storage capacity were performed under small mean effective stress changes in which elastic, infinitesimal strain was occurring. For the cases of measurements performed during the decreasing Pc part of the pressure cycle, compressibility measurements are elastic compressibilities, and are therefore directly applicable to the calculation of hydraulic diffusivity (Fig. 6(b)). For the measurements on the increasing Pc path in which a combined elastic-plastic compressibility has been used however, a compressibility value higher than the elastic matrix compressibility will have been used, resulted in underestimates of hydraulic diffusivity. Is it difficult to determine exactly the true elastic contributions to the compressibilities calculated in the experiments, so that a correction in the calculation of hydraulic diffusivies was not possible. However, the comparison between compressibilities during Pc increase in the first pressure cycle, and those from the decreasing Pc path and later pressure cycles, gives an impression of the impact of the plastic component on the first cycle increasing Pc compressibility data (Fig. 5(c)).

5.2 The hydromechanical response of slip zone gouge during fluid pressurization

The data presented in this paper show that the very fine gouge from a 10 cm wide principal displacement zone in the centre of the Median Tectonic Line fault core has a room temperature hydraulic diffusivity of around 1×10^{-7} to 4×10^{-7} m^2s^{-1} after compaction to $Pc - Pp$ values of 80 MPa and above. The properties of surrounding gouges, even ones adjacent to this principal displacement zone such as sample Ba, suggest much higher hydraulic diffusivities, typically 5×10^{-6} to 5×10^{-4} m^2s^{-1}. This section considers the implications of such hydraulic diffusivity data for models of fluid-controlled slip processes, particularly thermal pressurization. During earthquake slip, frictional heating of the pore fluid will cause a combination of three possible end-member responses: thermal expansion of the fluid resulting in expansion of the pores, thermal expansion of the fluid resulting in drainage out of the heated zone, and pressurization of the fluid if trapped within the pores of the heated zone. If thermal pressurization of the fluid occurs, the consequent reduction in effective normal stress could result in dramatic slip weakening (Sibson, 1973). Measured elastic compressibility values suggest that pore compressibility will be less than the compressibility of water at room temperature ($\beta_f = 4.277 \times 10^{-10}$ Pa^{-1}). Furthermore, fluid compressibility increases with temperature, so pores will certainly be less compressible than the water as it heats up. Poro-elastic expansion (the first of the three end-member responses) is therefore considered unlikely. The likelihood of thermal pressurization acting as a slip-weakening mechanism therefore balances on the relationship between the rate of frictional heating, and the rate at which a consequent fluid pressure pulse will be dissipated by fluid drainage from the heated zone. A first approximation is given by considering the undrained case. The decrease in effective normal stress on the fault can be calculated by considering the fluid pressure increase due to thermal expansion. For a thermal expansivity of water, α_t, of 1.5×10^{-3} K^{-1}, the fractional change in water density ($\Delta\rho_w/\rho_w$) due to a 30°C temperature rise, for example, will be 0.045. The rise in fluid pressure of the

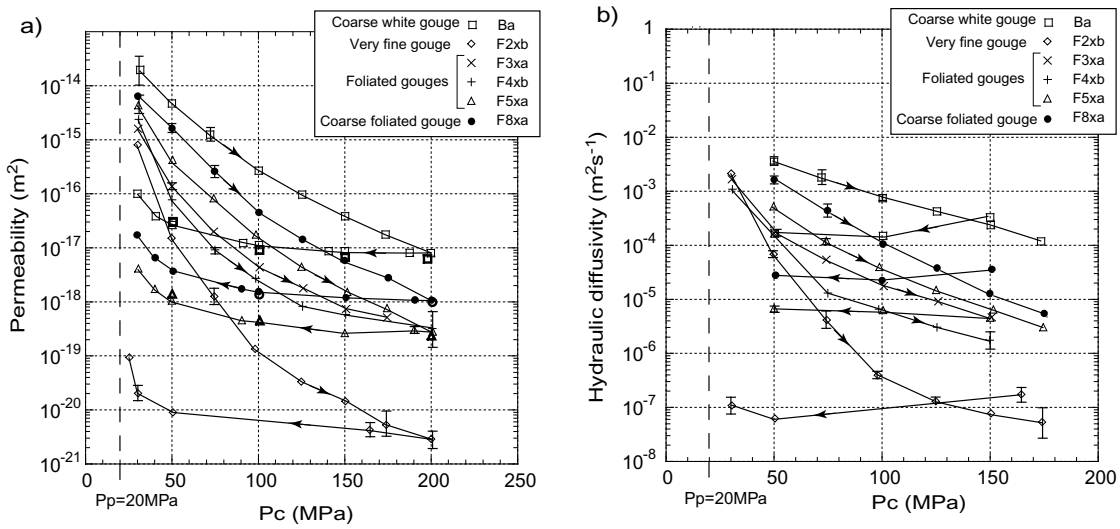

Fig. 6. Hydrodynamic properties of the fault gouges studied. (a) Permeability data, measured at a pore pressure of 20 MPa, except for the data are marked by bold open symbols which represent measurements at 30 MPa. Error bars were derived from standard deviations of repeated oscillation data. (b) Hydraulic diffusivity data derived using room temperature viscosity as discussed in the text. Error bars represent the added errors from permeability and from storage capacity measurements.

water, ΔP_w can be found as:

$$\Delta P_w = \frac{\Delta \rho_w}{\rho_w} \cdot \frac{1}{\beta_w}. \tag{3}$$

Assuming a compressibility of water of 4.3×10^{-10} Pa^{-1} the fluid pressure rise and consequent drop in effective normal stress is then 106 MPa.

For the fluid drainage problem, a simple calculation of the rate of fluid pressure dissipation from the centre of a low-permeability zone (half − width $= x$) to both edges is done as follows. This is provided only as a brief illustration of the use of fault zone hydraulic property data, and the reader is referred to recent modelling work for more rigorous solutions incorporating the frictional heating aspects of the problem (e.g. Vardoulakis, 2001; Andrews, 2003) in addition to the references provided in the introduction. From Darcy's law, the rate of fluid flux through an area A is expressed in terms of fluid pressure excess (ΔP_w) as:

$$\dot{q} = \frac{kA}{\eta} \frac{d\Delta P_w}{x} = D_h \beta_c A \frac{d\Delta P_w}{x}. \tag{4}$$

The rate volume loss of fluid from the centre of the zone, in both directions, is $2\dot{q}$. Given that the material around the very fine gouge slip zone of the Median Tectonic Line has much higher hydraulic diffusivity values, it is assumed here that this adjacent material will act in a drained manner. This is not necessarily the case, so the limits on thermal pressurization of the slip zone pore fluid here provide a conservative estimate for the conditions required for thermal pressurization. One condition on the occurrence of effective thermal pressurization is therefore that the hydraulic diffusion length be significantly smaller than the half-width of the low-permeability slip zone. The hydraulic diffusion length scale, or distance of propagation of a fluid pressure front d_h from a heat source at time t, can be related to the hydraulic diffusivity as (Lachenbruch, 1980):

$$d_h(t) = \sqrt{(4 D_h t)} \tag{5}$$

suggesting that over a 10 s period a fluid pressure front will propagate approximately 2 mm in each direction from the source (using $D_h = 1 \times 10^{-7}$ m^{2}s^{-1} for the very fine gouge slip zone). Given that the central slip zone is approximately 10 cm wide, although it does vary laterally along the outcrop examined, it is unlikely that the fluid pressure front will propagate beyond the low permeability slip zone during a rapid slip event.

The rate of pressure drop (dP_w/dt) due to the fluid escape is:

$$\frac{dP_w}{dt} = \frac{2\dot{q}}{\beta_f n V} = \frac{2 D_h \beta_c A \Delta P}{\beta_f x n V} \tag{6}$$

where nV is the pore volume in the central heated zone. If an approximation is used whereby the volume of the central slip zone (per unit length of fault) is considered to be that of the whole low-permeability zone, then $V = Ax$ so that Eq. (6) can be simplified:

$$\frac{dP_w}{dt} = \frac{2 D_h \beta_c \Delta P}{\beta_f n x^2}. \tag{7}$$

The pore compressibility is thought to be sufficiently lower than the fluid compressibility (Subsection 5.1) that a second approximation can be made, that the storage capacity is close to that due only to the compressibility of the fluid, so that Eq. (2) can be modified:

$$\beta_c = n \beta_f \tag{8}$$

and by substituting Eq. (8) into Eq. (7), a simple determination of the rate of fluid pressure loss is given:

$$\frac{dP_w}{dt} = \frac{2 D_h \Delta P}{x^2}. \tag{9}$$

The relationship in Eq. (9) is shown in Fig. 7(a), for the case of room temperature hydraulic conductivity (line 1).

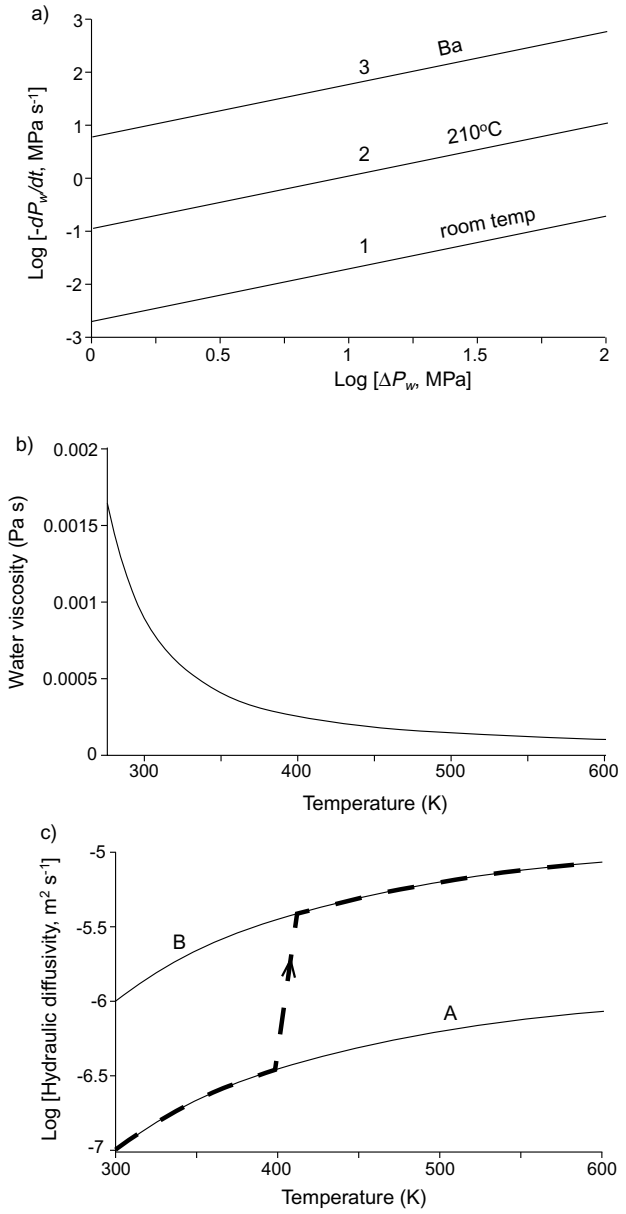

Fig. 7. The impact of temperature on gouge hydraulic diffusivity and rates of fluid pressure drop. (a) Fluid pressure drop rates vs. the magnitude of excess fluid pressure in the case of relatively incompressible pores, using Eq. (9), with $x = 0.01$ m, for three different hydraulic diffusivity cases: 1 - room temperature case using data from principal displacement zone gouge sample F2xb ($D_h = 1 \times 10^{-7}$ m^{2}s^{-1}); 2 - case at 210°C for sample F2xb ($D_h = 5.75 \times 10^{-6}$ m^{2}s^{-1}); 3 - room temperature case for coarse gouge sample Ba ($D_h = 3 \times 10^{-4}$ m^{2}s^{-1}). (b) The effect of temperature on water viscosity. (c) The impact of viscosity temperature-dependence on gouge hydraulic diffusivity for sample Fx2b, extrapolating from the room temperature case (deconfining pathway data in Fig. 6(b)), (curve A), and one order of magnitude higher, supposing this to represent gouge permeability once the structured water on clay grain surfaces has been driven off (curve B). The dashed line represents a possible real dependence of hydraulic diffusivity on temperature, taking both of these effects into account.

5.3 Likely hydrodynamic behaviour of slip zone gouge at elevated temperatures

This section discusses the impact of two consequences of heating on the hydrodynamic properties of the gouge. Firstly, the increase in temperature of the pore water will decrease its viscosity (Fig. 7(b)), resulting in the hydraulic diffusivity in the slip zone being higher at higher temperatures. From the room temperature calculations of hydraulic diffusivity (Fig. 6(b)), the corresponding higher temperature hydraulic diffusivities can be calculated from known water viscosity values. Unlike the effect of temperature, fluid pressure does not alter viscosity much, and is not considered here. Figure 7(c) (curve A) shows the increase in hydraulic diffusivity with temperature due to this decrease in water viscosity. Secondly, the structured water present on the surface of the clay grains in the gouge below approximately 120°C contributes to the relatively low permeability of clay rich gouges. Above this temperature, the structured water films may be driven off. Although the effect of this on water permeability has never been monitored at such temperatures, comparison of gas permeability data for naturally dry clay-rich gouges with water-saturated permeabilities suggests that permeability will increase by approximately 1 order of magnitude if the structured water layers are not present (Faulkner and Rutter, 2000). Removal of the structured water at 120°C would cause an increase in hydraulic diffusivity of one order of magnitude at this temperature (curve B, Fig. 7(c)).

The effect that these phenomena have on the dynamic slip-weakening effect during an earthquake depends upon the temperatures to which the water-saturated gouge is heated. In the case of a low permeability slip zone, Mase and Smith (1987) showed that the temperature rise would never be more than 20–50°C because initial thermal pressurization would decrease effective normal stress sufficiently to dramatically lower the rate of frictional heating. In such a case, the sequence of processes *frictional slip* $\rightarrow$ *heat generation* $\rightarrow$ *pore water pressurization* $\rightarrow$ *reduction in friction and rate of heating* is occurring on the fault, and the frictional temperature pulse is self-arresting. The impact of temperature on fluid viscosity, and therefore hydraulic diffusivity and the feasibility of thermal pressurization, is likely to be due to the initial ambient temperature more than by temperature rise. Hence the depth must be taken into consideration in calculations of the fluid pressure dissipation. An example is shown on Fig. 7(a) (line 2) of fluid pressure dissipation rate at a temperature of 210°C (corresponding to a depth of 7 km at a temperature gradient of 30°C/km).

5.4 Additional limitations provided by the constraints of fault zone structure

The gouge samples studied in this work were cored parallel to foliation. Data in Wibberley and Shimamoto (2003) show that at $Pc - Pp = 80$ MPa on the confining path, permeability perpendicular to foliation was more than one order of magnitude lower than permeability parallel to foliation. Similar anisotropy in permeability of clay gouges has been demonstrated in other works (e.g. Faulkner and Rutter, 1998). The estimates of gouge hydraulic diffusivity presented in this paper are therefore likely to be one order of magnitude higher than *in situ* hydraulic diffusivities perpendicular to the slip zone. The findings rely on propagation of slip only in the central slip zone gouge, which has sufficiently low permeability and hydraulic diffusivity for thermal pressurization to initiate. Outcrop observations of complex fault core zones (e.g. Wibberley and Shimamoto, 2003) suggest that ruptures can propagate obliquely or branch off a pre-existing slip plane in certain cases, and fault zone com-

plexity must be taken into consideration. If such a low-permeability zone is not laterally continuous, or the rupture plane propagates into another type of fault rock (such as at an asperity or point of interaction between a minor fault and the main slip plane), then fluid pressure may be released before effective pressurization can occur. A point where the slip plane propagates into coarser gouge or fractured cemented fault rocks in the wall rock to the principal displacement zone will experience higher fluid pressure dissipation rates. This is exemplified by line 3 in Fig. 7(a), using data on coarse gouge hydraulic diffusivity from sample Ba. A final point is that the state of the gouge zone may change through geological time, leading to different hydromechanical deformation mechanisms being favoured. Reworking of a gouge at a shallower conditions to its original depth of generation may create a greater porosity, thereby leading to fluidization. Overprinting of textures suggesting different hydromechanical mechanisms has recently been identified in gouge from the Nojima fault (Otsuki *et al.*, 2003) further underlining the importance of considering the deformation history of the gouge in understanding the hydromechanical behaviour of the fault.

6. Summary

This study investigates the laboratory fluid flow properties of fault gouges to find that:

1) Hydraulic diffusivity of the very fine clay gouge from the principal displacement zone of the MTL is around 1×10^{-7} m^2s^{-1} if subjected to a peak $Pc - Pp$ of 180 MPa at room temperature.

2) A fluid pressure pulse created by rapid frictional heating will remain trapped in the low-permeability slip zone, provided the gouge was initially at a pressure difference $Pc - Pp$ of at least several 10 s of MPa.

3) The trapped fluid pressure pulse will not cause pore dilation, but instead the rising fluid pressure will lead to a decreasing effective normal stress, resulting in a lower shear strength.

4) This process of dynamic shear strength reduction during earthquake slip could ultimately be limited by propagation of the rupture front into a high-permeability adjacent fault rock, such as at an asperity or branch point, leading to high dissipation rates of the excess fluid pressure.

Acknowledgments. This work has been carried out during receipt of a JSPS fellowship under the guidance of Professor T. Shimamoto, who is most sincerely thanked for his encouragement. The organisers and participants of the 'International Symposium on Slip and Flow Processes in and below the Seismogenic Regime' in Sendai, November 2001, are thanked for the opportunity to discuss this work. Tomochika Tokunaga and an anonymous reviewer are thanked for their helpful comments on the manuscript.

References

Andrews, D. J., A fault constitutive relation accounting for thermal pressurization of pore fluid, *J. Geophys. Res.*, 2003 (in press).

Birch, F., Compressibility; Elastic constants, in *Handbook of Physical Constants*, edited by S. P. Clark, The Geological Society of America Memoir 97, 97–173, 1966.

Caine, J. S., J. P. Evans, and C. B. Forster, Fault zone architecture and permeability structure, *Geology*, **24**, 1025–1028, 1996.

Chu, C. L., C. Y. Wang, and W. Lin, Permeability and frictional properties of San Andreas fault gouges, *Geophys. Res. Lett.*, **8**, 565–568, 1981.

Evans, J. P., C. B. Forster, and J. V. Goddard, Permeability of fault-related rocks, and implications for hydraulic structure of fault zones, *Journal of Structural Geology*, **19**, 1393–1404, 1997.

Faulkner, D. R. and E. H. Rutter, The gas-permeability of clay-bearing fault gouge at 20°C, in *Faulting, fault sealing and fluid-flow in hydrocarbon reservoirs*, edited by G. Jones, Q. Fischer, and R. J. Knipe. Geological Society Special Publication 147, 147–156, 1998.

Faulkner, D. R. and E. H. Rutter, Comparisons of water and argon permeability in natural clay-bearing fault gouge under high pressure at 20°C, *J. Geophys. Res.*, **105**, 16415–16426, 2000.

Fischer, G. J., The determination of permeability and storage capacity: pore pressure oscillation method, in *Fault Mechanics and Transport Properties of Rocks*, edited by B. Evans and T.-F. Wong, pp. 187–211, Academic Press, 1992.

Fischer, G. J. and M. S. Paterson, Measurement of permeability and storage capacity in rocks during deformation at high temperature and pressure, in *Fault Mechanics and Transport Properties of Rocks*, edited by B. Evans and T.-F. Wong, pp. 213–252, Academic Press, 1992.

Green, D. H. and H. F. Wang, Fluid pressure response to undrained compression in saturated sedimentary rock, *Geophysics*, **51**, 948–956, 1986.

Hickman, S., R. Sibson, and R. Bruhn, Introduction to special section: Mechanical involvement of fluids in faulting, *J. Geophys. Res.*, **100**, 12,831–12,840, 1995.

Ichikawa, K., Geohistory of the Median Tectonic Line of Southwest Japan, *Memoir of the Geological Society of Japan*, **18**, 187–212, 1980.

Klinkenberg, L. J., The permeability of porous media to liquids and gases, *Am. Petrol. Inst., Drilling and Production Practice*, **2**, 200–213, 1941.

Kobayashi, K. and 11 others, Distribution of fault rocks in the fracture zone of the Nojima Fault at a depth of 1140 m: Observations from the Hirabayashi NIED drill core, in *The Nojima Fault Zone Probe*, edited by N. Oshiman, T. Shimamoto, K. Takemura, and C. A. J. Wibberley, The Island Arc, 10, pp. 411–421, 2001.

Kranz, R. L., J. S. Saltzman, and J. D. Blacic, Hydraulic diffusivity measurements on laboratory rock samples using an oscillating pore pressure method, *International Journal of Rock Mechanics and Mining Sciences and Geomechanics Abstracts*, **27**, 345–352, 1990.

Lachenbruch, A., Frictional heating, fluid pressure, and the resistance to fault motion, *J. Geophys. Res.*, **85**, 6097–6112, 1980.

Lockner, D., H. Naka, H. Tanaka, H. Ito, and R. Ikeda, Permeability and strength of the Nojima core samples from the Nojima fault of the 1995 Kobe earthquake, in *Proceedings of the international workshop on the Nojima fault core and borehole data analysis*, edited by H. Ito, K. Fujimoto, H. Tanaka, and D. Lockner, USGS Open File Report 00-129, 147–152, 2000.

Mase, C. W. and L. Smith, Effects of frictional heating on the thermal, hydrological, and mechanical response of a fault, *J. Geophys. Res.*, **92**, 6249–6272, 1987.

Miller, S. A., Earthquake scaling and the strength of seismogenic faults, *Geophys. Res. Lett.*, **29**, GL014181, 2002.

Mizoguchi, K., T. Hirose, and T. Shimamoto, Permeability structure of the Nojima fault at Funaki, Hokudan-cho, Japan, *Gekkanchikyu-gougai (Earth Monthly)*, **31**, 58–65, 2000 (in Japanese).

Morrow, C. A., L. Q. Shi, and J. D. Byerlee, Permeability and strength of San Andreas gouge under high pressure, *Geophys. Res. Lett.*, **8**, 325–329, 1981.

Morrow, C. A., L. Q. Shi, and J. D. Byerlee, Permeability of fault gouge under confining pressure and shear stress, *J. Geophys. Res.*, **89**, 3193–3200, 1984.

Morrow, C. A., Z. Bo-Chong, and J. D. Byerlee, Effective pressure law for permeability of Westerly Granite under cyclic loading, *J. Geophys. Res.*, **91**, 3870–3876, 1986.

Ohtani, T., H. Tanaka, K. Fujimoto, T. Higuchi, N. Tomida, and H. Ito, Internal structure of the Nojima Fault zone from the Hirabayashi GSJ drill core, in *The Nojima Fault Zone Probe*, edited by N. Oshiman, T. Shimamoto, K. Takemura, and C. A. J. Wibberley, The Island Arc, 10, pp. 392–400, 2001.

Otsuki, K., N. Monzawa, and T. Nagase, Fluidization and melting of fault gouge during seismic slip: Identification in the Nojima fault zone and implications for focal earthquake mechanisms, *J. Geophys. Res.*, 2003 (in press).

Scholz, C. H. and S. H. Hickman, Hysteresis in the closure of a nominally flat crack, *J. Geophys. Res.*, **88**, 6501–6504, 1983.

Seront, B., T.-F. Wong, J. S. Caine, C. B. Forster, R. L. Bruhn, and J. T. Fredrich, Laboratory characterization of hydrodynamical properties of a seismogenic normal fault system, *Journal of Structural Geology*, **20**,

865–881, 1998.

Sibson, R. H., Interactions between temperature and pore-fluid pressure during earthquake faulting and a mechanism for partial or total stress relief, *Nature*, **243**, 66–68, 1973.

Tadokoro, K., K. Nishigami, M. Ando, N. Hirata, T. Iidaka, Y. Hashida, K. Shimakaki, S. Ohmi, Y. Kano, M. Koizumi, S. Matsuo, and H. Wada, Seismicity changes related to a water injection experiment in the Nojima Fault zone, in *The Nojima Fault Zone Probe*, edited by N. Oshiman, T. Shimamoto, K. Takemura and C. A. J. Wibberley, The Island Arc, 10, pp. 235–243, 2001.

Takagi, H., Implications of mylonitic microstructures for the geotectonic evolution of the Median Tectonic Line, central Japan, *Journal of Structural Geology*, **8**, 3–14, 1986.

Vardoulakis, I., Thermo-poro-mechanical analysis of rapid fault deformation, in Powders and Grains, Proceedings of the 4th International Conference on Micromechanics of Granular Media, Sendai, Japan, 2001.

Wibberley, C. A. J. and T. Shimamoto, Internal structure and permeability of major strike-slip fault zones: the Median Tectonic Line in Mie Prefecture, Southwest Japan, *Journal of Structural Geology*, **25**, 59–78, 2003.

Wood, D. M., Soil behaviour and critical state soil mechanics, 462 pp., Cambridge University Press, Cambridge, 1990.

Zhang, S. and S. F. Cox, Enhancement of fluid permeability during shear deformation of a synthetic mud, *Journal of Structural Geology*, **22**, 1385–1393, 2000.

Zhu, W. and T.-F. Wong, The transition from brittle faulting to cataclastic flow: permeability evolution, *J. Geophys. Res.*, **102**, 3027–3041, 1997.

C. A. J. Wibberley (e-mail: cwibber@ip.media.kyoto-u.ac.jp)